Tailored height gradients in vertical nanowire arrays via mechanical and electronic modulation of metal assisted chemical etching

Supporting Information

M.A. Otte[1], V. Solis-Tinoco[1], P. Prieto[2], X. Borrisé[1], L.M Lechuga[1], M.U González[2], and B. Sepulveda[1*]

Index

S1. Formula: Spring constant of perforated membranes

S2. Formula: Incremental change of perforated membrane area after mechanical deformation

S3. Examples of uncontrolled metal membrane rupture during MACE

S4. High resolution SEM images to determine *s* parameter in F_{vdW}

S5. Estimation of van der Waals pressure and Hamaker constant

S6. Fick's law of diffusion during MACE

S7. Examples of nanopillars with different geometries

S8. Examples of pattern transfer of nanopillar arrays with height gradients to polymers

S1. Formula: Spring Constant of Perforated Membranes

In the elastic regime, the spring constant of a circular perforated metal membrane subjected to a homogeneous load is given by [1]:

(Eq. S1.1) $$k = \frac{64\,\pi\,E\,t^3}{3\,D^2(1-\nu^2)}(1-\phi)$$

Herein, E and ν are the Young´s Modulus and Poisson ratio of the metal, respectively, t the metallic layer thickness, D the diameter of the membrane, and ϕ is the filling factor that represents the relative perforated area of the membrane (normalized with respect to 1). The filling factor is defined as the fraction of the area occupied by the nanoholes with respect to the total array area. If $\#_{nh}$ is the number of circular nanoholes (diameter D_{nh}) present in a perforated circular membrane with diameter D, the filling factor ϕ can be expressed as:

(Eq. S1.2) $$\phi = \frac{\#_{nh}\times D_{nh}^2}{D^2}$$

In this expression, $\#_{nh}$ can be approximated by multiplying the fraction of a circular area $A_{membrane}$ with respect to the area of a square with dimensions $A_{square} = D^2$, with the total number of nanoholes (spaced with a periodicity P) that fit inside this square $\#_{square}$:

(Eq. S1.3) $$\#_{nh} \approx \frac{A_{membrane}}{A_{square}}\times\#_{square}$$

After filling in the expression for each quantity, this equation can be rewritten as follows:

(Eq. S1.4) $$\#_{nh} \approx \frac{\frac{\pi}{4}D^2}{D^2}\times\left(\frac{D}{P}+1\right)^2$$

Then, since typically $\frac{D^2}{P^2} \gg \frac{2D}{P}+1$, a final approximation[1] can be made, leaving:

(Eq. S1.5) $$\#_{nh} \approx \frac{\pi}{4}\times\left(\frac{D}{P}\right)^2$$

Hence, insertion of this expression into the formula that defines ϕ, finally gives:

(Eq. S1.6) $$\phi \approx \frac{\pi}{4}\times\left(\frac{D_{nh}}{P}\right)^2$$

After insertion of this term in the expression for the spring constant, this latter parameter can be expressed as:

(Eq. S1.7) $$k = \frac{64\,\pi\,E\,t^3}{3\,D^2(1-\nu^2)}\times\left(1-\frac{\pi D_{nh}^2}{4P^2}\right)$$

---

[1] *This approximation introduces an error that depends on the values of D and P. This error is maximized for the smallest array diameter with the highest periodicity, that is, D=5μm and P=500nm, resulting in an error of approximately 20%. On the other extreme, the minimal value of this error corresponds to the largest array with the smallest periodicity: D=40μm and P=300nm. In this case, the introduced error is as small as 1.5%.*

S2. Formula derivation: Incremental change of perforated membrane area after mechanical deformation

The mechanical deformation of the metal membrane can be analyzed by calculating the incremental change in area *dA* of the perforated metal membrane after it has been subjected to mechanical deformation. For simplicity, the area of the perforated metal membrane *before* mechanical deformation is denoted as A_1, while the area *after* mechanical deformation is denotes as A_2. Now, *dA* can be expressed as:

(Eq. S2.1) $$dA[\%] = \left(\frac{A_2}{A_1} - 1\right) \times 100\%$$

For an array with diameter *D* and filling factor ϕ, A_1 can be written as:

(Eq. S2.2) $$A_1 = (1 - \phi) \times \frac{\pi D^2}{4}$$

On the other hand, the membrane geometry *after* mechanical deformation can be approximated as a spherical capped geometry. This type of geometry, in the absence of nanoholes, has a surface area given by $A = \pi \times \left(\frac{D^2}{4} + H_{center}^2\right)$. Hence, when perforated (and assuming that the nanoholes retain their dimensions, that is, their cross-sectional area remains unchanged), then A_2 can be approximated as:

(Eq. S2.3) $$A_2 \approx (1 - \phi) \times \frac{\pi D^2}{4} + \pi H_{center}^2$$

Now, the fraction A_2 / A_1 can be written as:

(Eq. S2.4) $$\frac{A_2}{A_1} \approx 1 + \frac{4 \times H_{center}^2}{(1-\phi) \times D^2}$$

With this expression, dA is reduced to:

(Eq. S2.5) $$dA[\%] \approx \frac{4 \times H_{center}^2}{(1-\phi) \times D^2} \times 100\%$$

S3. Examples of uncontrolled metal membrane rupture during MACE

SEM images (Fig. S3 a-d) of 20 nm thick perforated gold membranes that were subjected to an overload of mechanical stress during MACE for times longer than 2 minutes. The overload resulted in the uncontrolled rupture of the membrane and a subsequent chaotic MACE process. As can be observed in Fig. S3b, the mechanical rupture and associated release of the mechanical stress allows the local acceleration of the MACE process in arrays where F_{mech} and F_{vdW} are in the same order of magnitude. The dashed red lines define the regions along which the membrane rupture occurred.

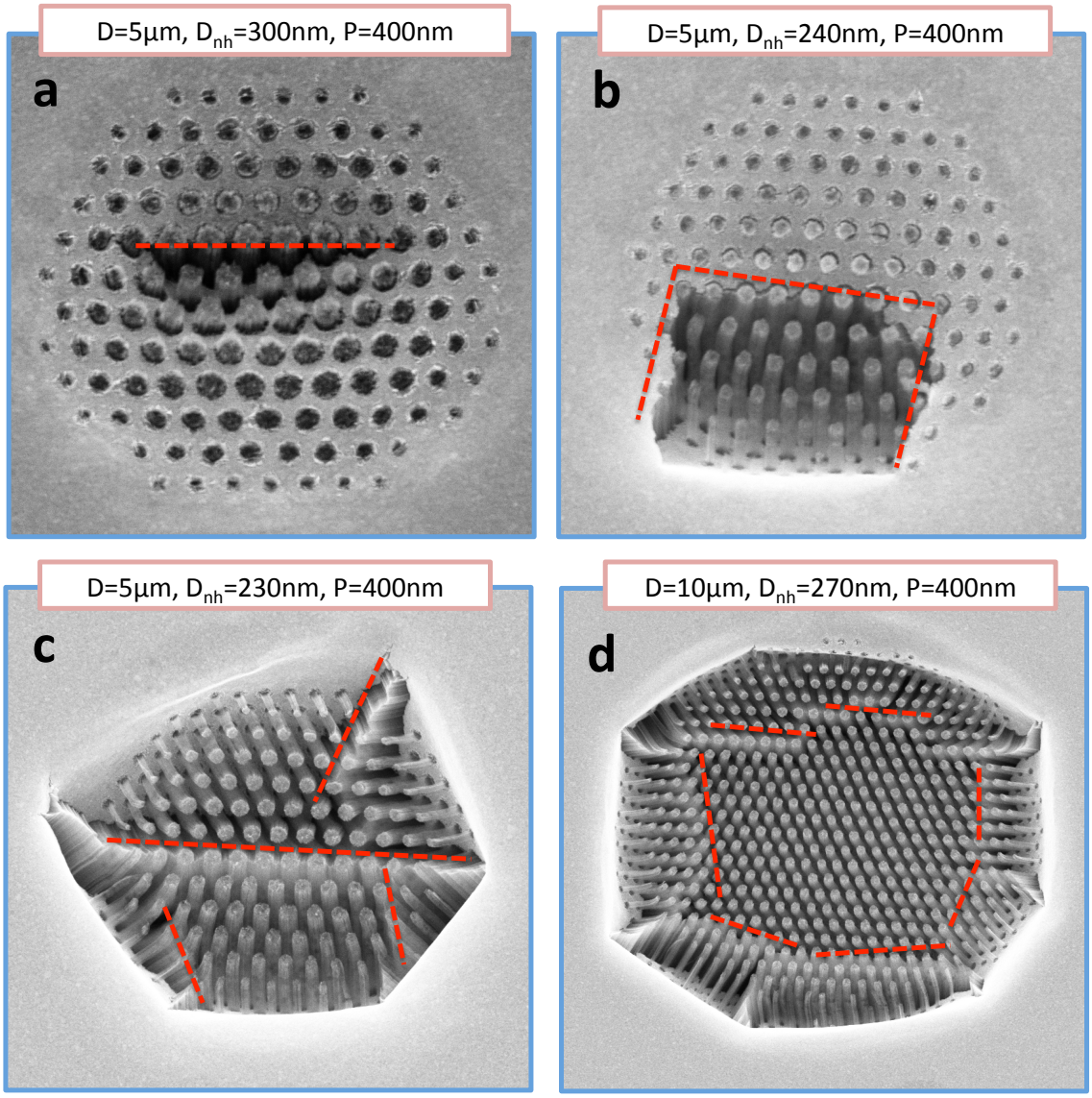

Fig. S3 Nanopillar arrays after gold membrane rupture. (**A**) Array representing the rupture along only one line. (**B**) Membrane rupture in three regions, given rise to a part of the metal membrane that can be freely deformed like a hinge. In this region the release of mechanical tension accelerates the MACE process. (**C** and **D**) Arrays with several uncontrolled rupture region leading to very fast MACE rates.

S4. High resolution SEM images to determine s parameter in F_{vdW}

Figure S4 displays high resolution secondary electron (**A** and **C**) and back scattering (**B** and **D**) SEM images of irregular shape nanopillars to determine the separation distance *s* between the gold membrane and the substrate during MACE. The distance *s* between the end of the metal membrane and the lateral surface of the nanopillars varies in the range from 7 to 10 nm. Back scattering images clearly show how the nanopillar shape follows the irregular shape of the nanohole in the metal membrane.

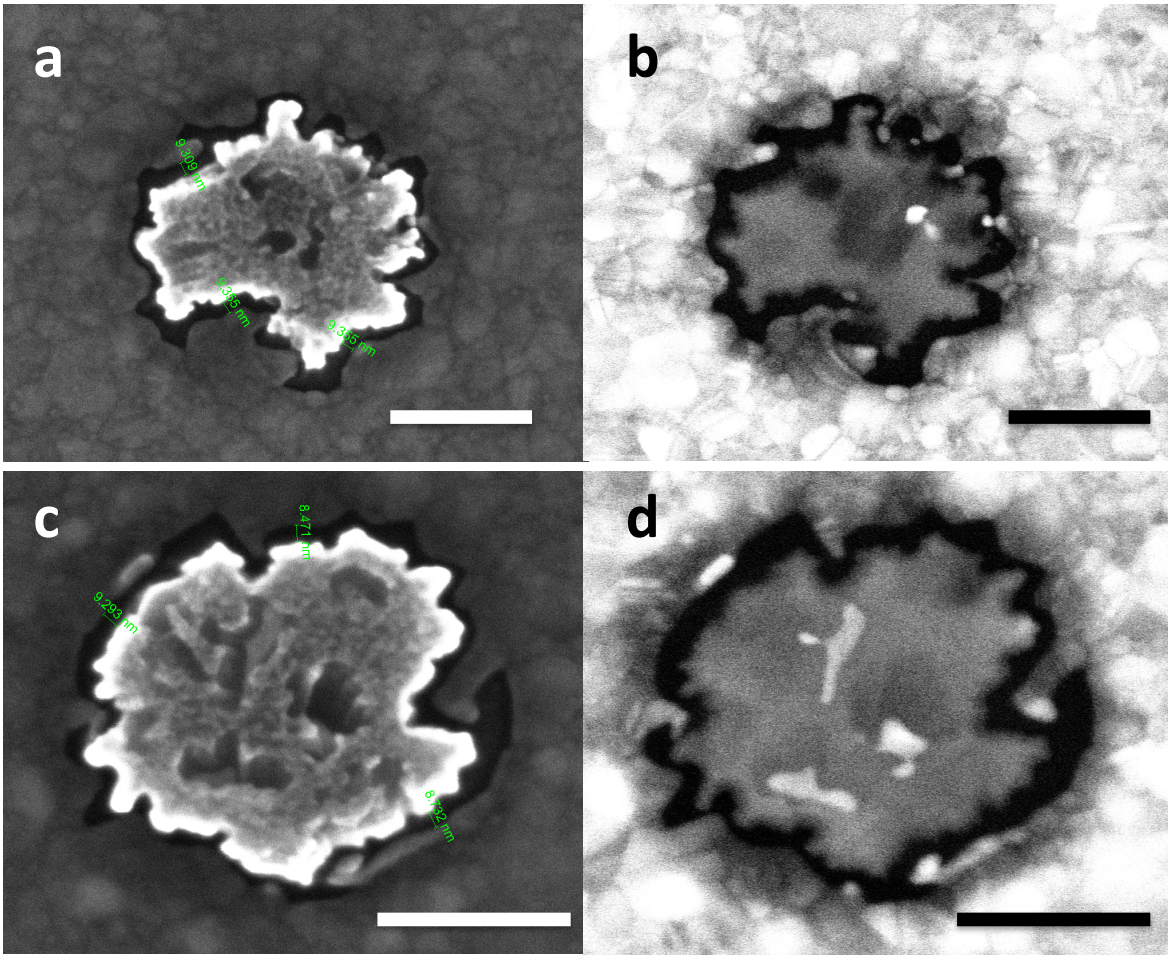

Fig. S4 High resolution SEM images of 20 nm thick metal membranes and the obtained nanopillars to determine the factor *s* in F_{vdW}. (**A**) and (**C**) Secondary electron images. (**B**) and (**D**) SEM images using back scattered electrons. The dark contour in all the images is the space comprised between the metal film and the silicon pillar. The shape of the pillar clearly follows the irregular shape of the nanohole. The scale bars represent 100 nm.

S5. Estimation of van der Waals pressure and Hamaker constant

A careful selection of the mechanical properties of the perforated membrane enables the generation of a mechanical restoring force that can match the van der Walls force during the etching process. An example is represented in Fig. S5, where we compare mechanically connected and disconnected arrays in a 50 nm gold film after 8 minutes etching. In Fig. S5a, the mechanical force is able to reach the van del Waals force when the etching depth at the center is H_{center} = 380 nm. At this point the catalytic reaction is stopped due to the impossibility to continue the mechanical deformation of the metal membrane, thereby preventing further h^+ injection. In contrast, in the fully mechanically disconnected case, the membrane can freely continue the etching process leading to long (*ca.* 2 μm) pillars.

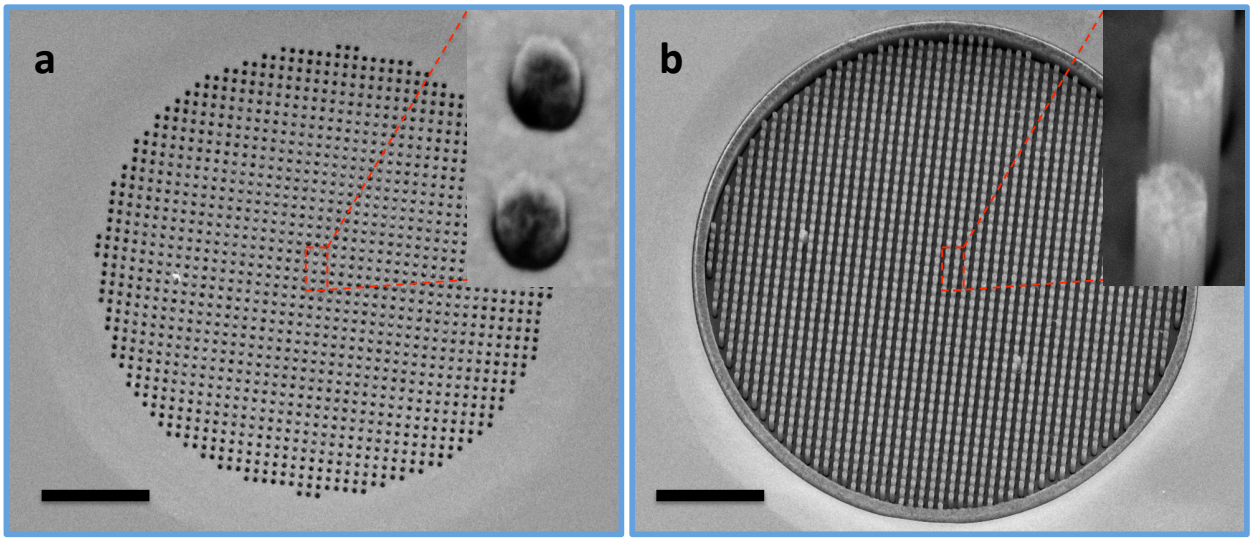

Fig. S5. Comparison of the etching depth after 8 minutes etching in a fully mechanically connected (**A**) and disconnected (**B**) arrays in a 50 nm gold film, being D = 20 μm, P = 400 nm, D_{nh} = 200 nm. Figure (**A**) shows the capacity to reach the equilibrium between F_{vdW} and F_{mech}. The scale bars represent 5 μm.

The capacity to reach the force equilibrium (*i.e.* $F_{vdW} = F_{mech}$) enable us the determination of the van der Waals pressure as:

Eq. S5.1
$$\sigma_{vdW} = \frac{F_{mech}}{A(1-\phi)}$$

Considering the geometrical pattern in the membrane of Fig. S5a and Eq. 2, we can estimate that $\sigma \approx$ 2 kPa. If we assume a mean separation distance s = 9 nm during etching (Fig. S4), we can extract that the Hamaker constant under these etching conditions is C = 2.7 10^{-20} J, very close to that expected from the Au/SiO_2 interaction. Both the large value of s and the extracted C confirm that the hole injection current is highly amplified and that the etching process follows the intermediate formation of a SiO_2 layer.

S6. Fick´s law of diffusion during MACE

According to Fick's law of diffusion, the flow of mass of a substance per unit area per unit time J is given by:

(Eq. S6.1) $$J = -Q\frac{dK}{dx}$$

where Q is the diffusion coefficient, and $\frac{dK}{dx}$ the derivative of the concentration as a function of the coordinate x. In the MACE case, the diffusion occurs across the metal membrane. If the edge to edge distance between nanoholes is d_{ee}, we can assume that HF concentration at the nanohole entrance is the same as that of the etching solution and that the concentration at the end of the carved region in the silicon is zero (see Fig. S6). As a result, the derivative can be approximated by:

(Eq. S6.2) $$\frac{dK}{dx} \approx \frac{K_{HF}\left(x=\frac{d_{ee}}{2}\right)-K_{HF}(x=0)}{\frac{d_{ee}}{2}-0} \approx -\frac{2[HF]}{d_{ee}}$$

At the same time, J can be expressed as:

(Eq. S6.3) $$J = \rho_{Si}\vartheta$$

where ρ_{Si} is the mass density of silicon, and ϑ the etching rate. The etching rate ϑ approximately exhibits the following dependence on d_{ee}:

(Eq. S6.4) $$\vartheta \approx \frac{2\,Q\,[HF]}{\rho_{Si}d_{ee}}$$

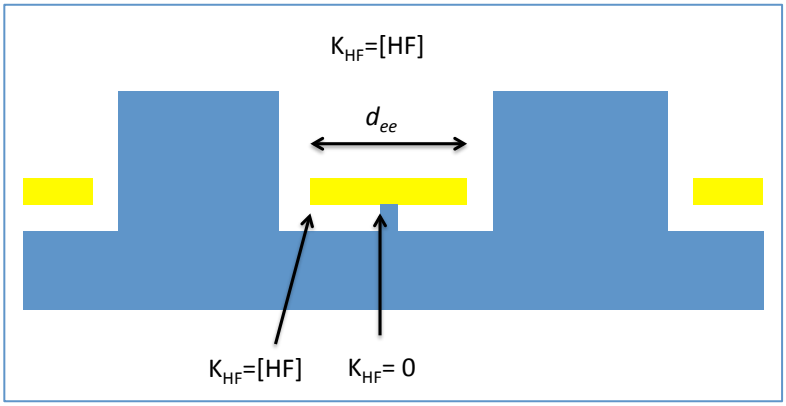

Fig. S6 Schematic of the MACE process underneath the metal membrane to determine the etching rate dependence on the edge-to-edge distance between nanoholes.

S7. Examples of nanopillars with different geometries

SEM images (Fig. S7 a-d) of nanopillar arrays (D=10μm), each characterized by different nanopillar geometries, showing that the nanopillar design is not limited to circular cross-sectional geometries. The images show (a) rectangular rod-like pillars, (b) dimers based on circular nanopillars, (c) nanopillars with "open-donut" shapes, and (d) pillars with cross-like structures.

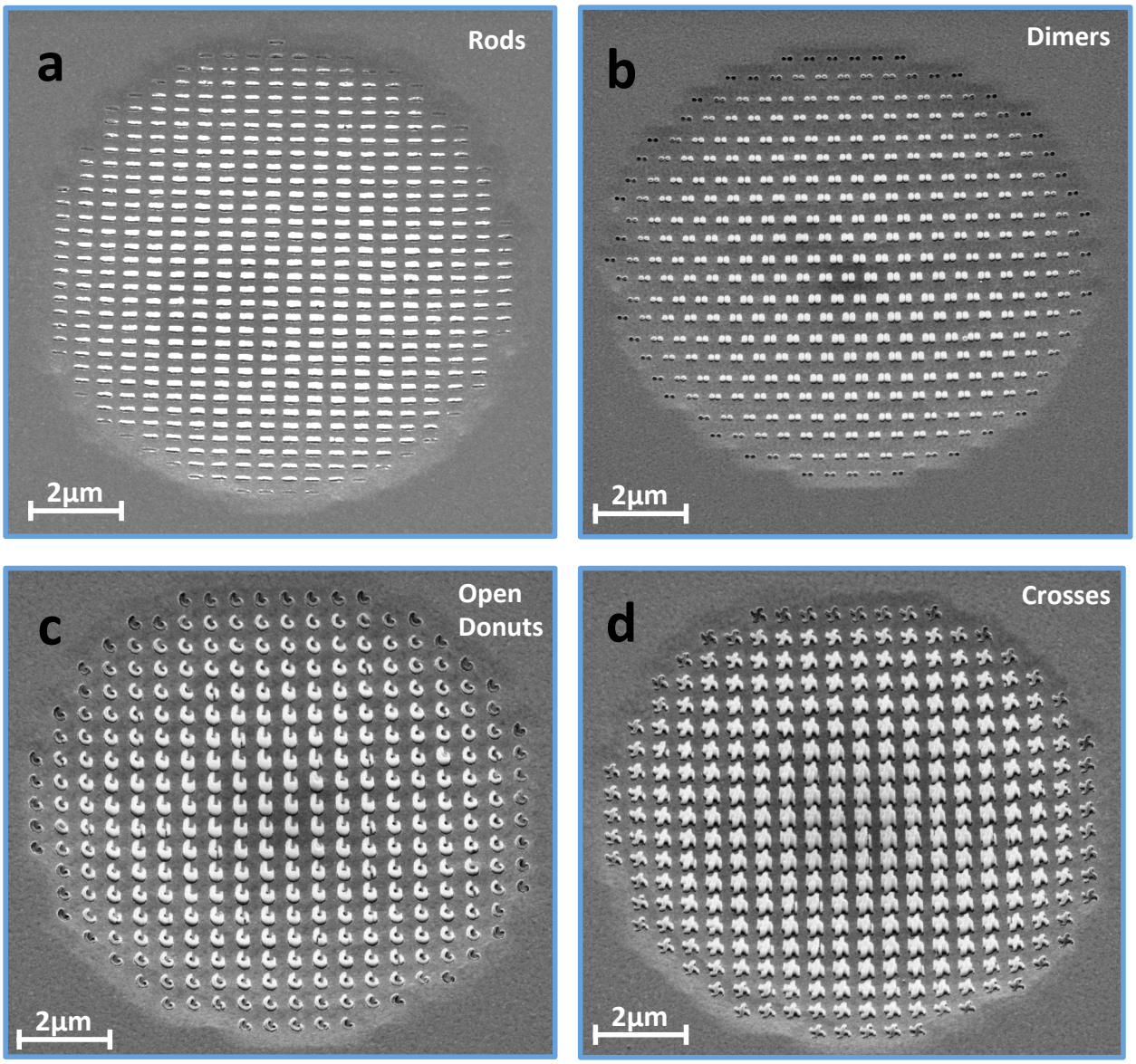

Fig. S7 SEM images of nanopillar arrays showing different cross-section geometry and height gradients in the radial direction.

S8. Examples of pattern transfer of nanopillar arrays with height gradients to polymers

SEM images (Fig. S8 a-b) of polymer nanopillar arrays obtained via pattern transfer. To fabricate these arrays, Si nanopillar arrays as those discussed throughout the manuscript are initially used as master for nanoimprint replica-molding. A PDMS negative mold is created, that is subsequently used to cast the polymer nanopillar arrays. As can be seen from these SEM images, depending on the stiffness of the employed polymer, the nanopillar arrays are much more rigid (Fig S8a) or more bendable (Fig S8b).

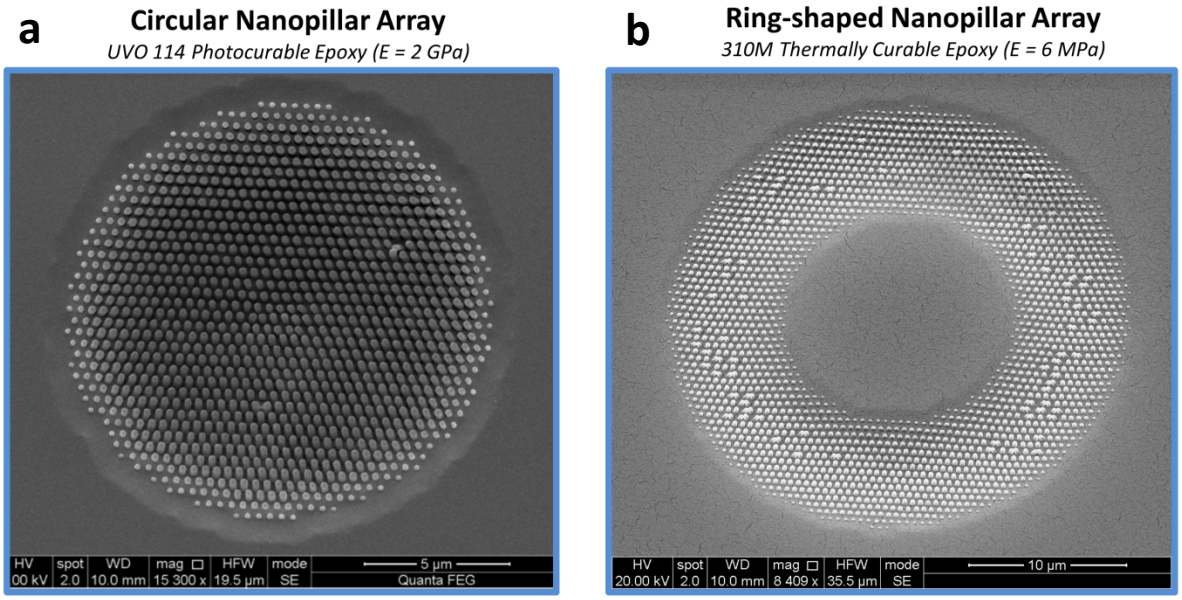

Fig. S8 SEM images of polymer nanopillar arrays with height gradients replicated from Si nanopilar masters. (**A**) UVO-114 polymer with E = 2 GPa. (**B**) 310M polymer with E = 6 MPa.

References

1. Nguyen N. T., Wereley S. T. *Fundamentals and Applications of Microfluidics*. Artech House, 2002.